Microshape and rough-surface analysis by fringe projection

Klaus Leonhardt, Ulrich Droste, and Hans. J. Tiziani

A fringe-projection system for microscopic applications, fringe-projecting microscopy, is developed and analyzed. Projection of the grating and imaging of the fringe system, modulated by the surface, are accomplished by the same high-aperture objective. The spectrum of the grating is spatially filtered and projected into the aperture with a lateral shift, which leads to a telecentric projection under oblique incidence and telecentric imaging. Topographies of specularly as well as diffusely reflecting surfaces can be obtained. The measurement of highly rough surfaces is described together with preprocessing steps. The resulting intensity distribution of the fringes is analyzed. Formulas for vertical and lateral resolution, measuring range, and dynamic range, based on noise considerations, are presented and verified by topographies of technical surfaces.

Key words: Fringe-projecting microscopy, topometry, fringe analysis, microshape analysis, rough-surface analysis, surface sensor, resolution, noise.

1. Introduction

Three-dimensional shape analysis by fringe projection is becoming important in optical metrology, robot vision, industrial inspection, and medicine. Besides triangulation, fringe projection has become an important technique. Diffusely reflecting macroscopic objects can be measured[1–3] by the projection of an interferometric fringe pattern[4,5] or an incoherent grating pattern[1] under oblique incidence onto the object. The pattern is observed by an imaging system with a camera, the optical axis of the imaging system being normal to the mean tangential plane to the object and forming an angle β with respect to the axis of the projection system. As in the case of light-sectioning microscopy,[6] the straight lines of the pattern are deformed by the shape of the object. The phase of the local fringe displacement is analyzed by methods of interferogram analysis.[7–10] These methods work as long as the surfaces of the objects are diffusely reflecting.

Microscopic objects are not restricted to diffusely reflecting surfaces only. Typical objects are polished metal, glass and semiconductor surfaces, diamond turned-metal surfaces, lacquer surfaces, and even highly reflecting mirrors. On the other hand, rough surfaces like sheet metal, ground- and turned-metal surfaces, plastics, ceramics, and even biological surfaces have to be topographed. Only a symmetrical configuration with $\pm\beta$ for the directions of projection and imaging (Fig. 1), including the case of regular reflection for smooth objects and an optimum range of scattering angles for rough surfaces, covers all these requirements.[11] Here we describe and analyze the measurement of microshape and roughness with fringe-projecting microscopy (FPM) in symmetric, single-aperture configurations. We use the term single-aperture configuration for the case in which both the projection and the imaging of the grating are accomplished through the same aperture. With this configuration a compact instrument with high lateral and vertical resolution can be realized. It is shown that their ranges of resolution partially overlap with the resolution of interference microscopy. In contrast to interference microscopy, FPM allows for topographies even of rough surfaces. It is much more robust and easier to handle.

2. Principle of Fringe Projection in a Single-Aperture System

The spatially filtered spectrum of a binary line grating is projected onto pupil plane EP (Fig. 1) of microscope objective MO with aperture D. By spatial filtering, only the -1st, 0th, and $+1$st orders of the spectrum are transmitted (Fig. 2). The spec-

The authors are with the Institut fuer Technische Optik, Universitaet Stuttgart, Pfaffenwaldring 9, 70569 Stuttgart, Germany.

Received 5 March 1993; revised manuscript received 17 February 1994.

0003-6935/94/317477-12$06.00/0.

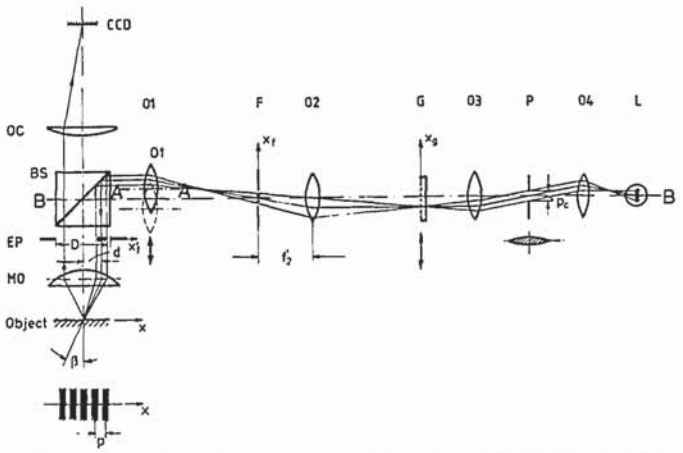

Fig. 1. Schematic of fringe-projecting microscopy in a symmetric, single-aperture configuration: CCD, image plane with camera; OC, tube lens; O1, relay lens for the grating spectrum; F, filtering plane of the grating spectrum; G, grating plane; P, entrance pupil with lens-shaped aperture; L, lamp; BS, beam splitter; EP, aperture plane of objective MO with the spectrum of the projected grating; MO, microscope objective.

trum is shifted off axis by distance d so that the principal ray of the zero order forms an angle β with the optical axis of the microscope objective in the object space. As the back focal plane of microscope objectives is not accessible physically for spatial filtering, the filtering is done in plane F, which is conjugate to EP by beam splitter BS and lens O1. This secondary pupil is easily accessible for filtering manipulations. The amount of the off-axis shift d is matched to the pupil diameter D in such a way that the outer first order of the grating spectrum can pass the pupil, allowing for sufficient clearance for lateral displacement or dispersion of the spectrum of the backtraveling light reflected from inclined- or rough-surface elements.

In our FPM arrangement both the entrance pupil of the imaging system and the exit pupil of the grating projection system lie at infinity. With this telecentric arrangement there are no problems with compensation for variations of sensitivity [see Eq. (11)] over the object field or nonlinearities in the relation of phase to height, as was reported from nontelecentric macroscopic fringe projection.[1–3] If the grating is adjusted perpendicularly to the optical axis in plane G, the image plane of the projected grating is oriented parallel to the x, y plane of the object, and the fringe contrast is constant over the object.

The spectrum is formed in focal plane F of lens O2 from a binary grating located in plane G. The grating is illuminated by a tungsten halogenide lamp, L, through lenses O4 and O3. A lens-shaped aperture in plane P (Fig. 1) of the illuminating system with radii matched to the radius of EP optimizes the light flux (Fig. 2). In addition, because of this shape, spatial coherence in the direction parallel to the projected fringes is lower than in the direction perpendicular to the fringes. The reduction of spatial and temporal coherence helps in the reduction of local topography errors that are due to the random intensity modulation caused by roughness and discontinuities. Objective O_c and a CCD interline transfer camera with 756 × 581 picture elements complete the optical system.

3. Intensity of the Projected Grating Lines and Fringe Formation

To calculate the intensity distribution of the projected grating lines on the object, we replace the optical arrangement with a simplified model, Fig. 3, in which the intermediate imaging step from pupil plane F of Fig. 1 to entrance pupil EP of objective O1 is omitted. Apart from a scaling factor, this has no influence on the analysis. For simplicity coherent light is assumed. A binary amplitude grating with period p_g and rectangular opaque bars of width $p_g/2$ are obliquely illuminated by a plane wave front with $\sin\beta_g = -(f_2/f_{om})\sin\beta$. In the grating plane the complex amplitude $u(x_g)$ can then be written as

$$u(x_g) = \exp\left(-i2\pi x_g \frac{d}{\lambda f_2}\right)\left[\sum_{n=-\infty}^{n=+\infty} \delta(np_g - x_g) * \mathrm{rect}\left(\frac{2x_g}{p_g}\right)\right] \times \mathrm{rect}\left(\frac{x_g}{w_g}\right), \quad (1)$$

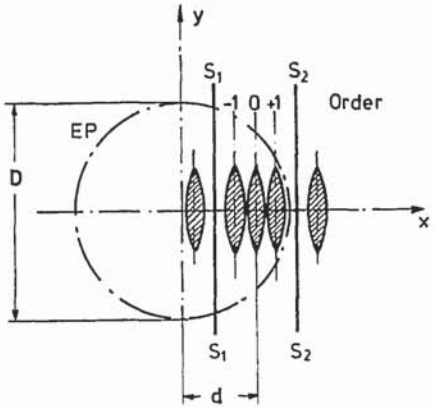

Fig. 2. Grating spectrum in aperture EP. The −1st, 0th, and +1st orders of the grating spectrum are transmitted (hatched lens-shaped areas). The ±2nd orders are practically missing, and orders higher than ±2 are filtered out by the slit in plane F. The position of the borders of the slits are marked by S_1–S_1 and S_2–S_2.

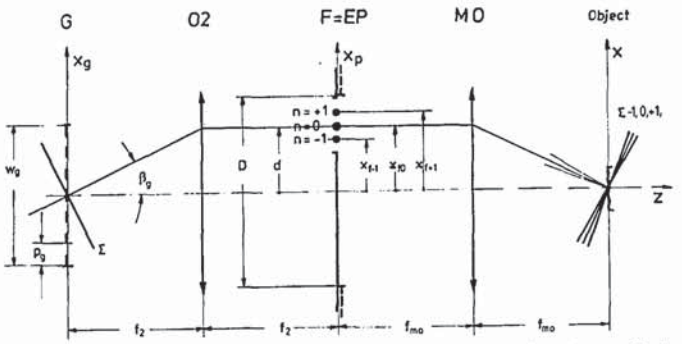

Fig. 3. Simplified arrangement of the grating projection and the spatial filtering showing the parameters of the theoretical analysis. Relay lens O1 is omitted for simplicity: G, grating plane; F, filtering plane conjugated to aperture plane EP; D, aperture diameter of MO; d, transversal shift of the grating spectrum.

where f_2 is the focal length of O2, p_g is the grating period and w_g is the width of the grating aperture. The symbol $*$ denotes convolution, $\delta(x)$ is the Dirac delta function, and $\mathrm{rect}(x)$ is the rectangle function. The complex amplitude of the grating spectrum with spatial frequency f_x is given by the Fourier transform $\tilde{u}(f_x)$ of $u(x_g)$:

$$\tilde{u}(f_x) = \delta(f_x - f_{x0}) * \left[\sum_{i=-\infty}^{+\infty} \frac{1}{p_g}\delta\left(f_x - \frac{i}{p_g}\right)\frac{p_g}{2}\,\mathrm{sinc}\left(\frac{f_x p_g}{2}\right)\right] * w_g\,\mathrm{sinc}(f_x w_g), \tag{2}$$

where $f_{x0} = d/(\lambda f_2)$. For $w_g \gg p_g$ the convolution with $\mathrm{sinc}(f_x w_g)$ can be neglected and the -1.0, 0, $+1.0$ orders of the grating spectrum can be isolated by the slit S_1S_1–S_2S_2 (Fig. 2):

$$\tilde{u}(f_x) = \frac{w_g}{2}[s\delta(f_x - f_{x-1}) + s_0\delta(f_x - f_{x0}) + s\delta(f_x - f_{x+1})], \tag{3}$$

where $f_{xi} = -x_{fi}/\lambda f_2$, $i = \cdots -1,\ 0,\ +1 \cdots$ are the spatial frequencies of the spectral orders, x_{fi} are their physical displacements in pupil EP, and

$$s_0 = \mathrm{sinc}(0) = 1,$$
$$s_1 = s_{-1} = s = \mathrm{sinc}(0.5) = 0.637. \tag{4}$$

Equation (3) describes a special form of three-beam interference. The complex amplitude in the object plane after reflection on the surface with height variations $h(x)$, Fig. 4, is

$$u(x) = \frac{w_g}{2}\sum_{j=-1}^{1} s_j \exp\left\{ik\left[\left(\frac{d}{f_{MO}} - \frac{\lambda}{p_g}j\right)x - 2\cos\beta_j h(x)\right]\right\}. \tag{5}$$

where f_{MO} is the focal length of the microscope objective. Thus the formation of the filtered grating lines can be described by triple plane waves, Fig. 4, each modulated by local path difference OPD = $2h(x)\cos\beta_i$, $\beta_0 = \beta$, $\beta_{+1} = \beta + \lambda/p$, $\beta_{-1} = \beta - \lambda/p$; $k = 2\pi/\lambda$, and $p = p_g f_{MO}/f_2$ is the period of the projected grating on the object. To include the influence of aberrations and defocusing, we specify the wave-front aberrations in pupil EP as phase contributions ϕ_j, $j = -1, 0, +1$, to the complex amplitude of Eq. (3):

$$\phi_j = kW(x_f)\delta(x_f - x_{fj}), \tag{6}$$

where $W(x_f)$ is the wave-front aberration relative to a reference sphere centered on the paraxial focus as a function of the relative height in EP. The radius of the border of EP is $D/2$, and f_{xm} is the corresponding maximum spatial frequency. For defocusing, we specify W_j as

$$W_j = x_{rj}^2\, W_{20}, \qquad j = -1, 0, +1,$$
$$x_{rj} = \frac{x_{fj}}{D/2}, \tag{7}$$

where W_{20} is the aberration at the border of the EP. This procedure could be generalized to spherical aberration by the addition of contributions with x_{rj}^4 W_{40} to W_j in Eqs. (7):

$$u(x) = \frac{w_g}{2}\sum_{j=-1}^{1} s_j \exp\left\{ik\left[\left(\frac{d}{f_{MO}} - \frac{\lambda}{p_g}j\right)x - 2\cos\beta_j h(x) + W_j\right]\right\}. \tag{8}$$

For the intensity distribution $I(x, Y) = u^*(x, Y)u(x, Y)$, we find, after straightforward calculations,

$$I(x, Y) = I_0(1 + 2s\cos\alpha)^2 = I_0(1 + 2s^2 + 4s\cos\alpha + 2s^2\cos 2\alpha), \tag{9}$$

$$\alpha(x) = \frac{2\pi}{p}[x - 2h(x)\sin\beta] + k\Delta W,$$
$$\Delta W \approx (W_3 - W_1)/2. \tag{10}$$

The approximation for ΔW holds for $d \gg \lambda f_{MO}/p$. Thus only the second harmonic is present in the intensity distribution. The intensity distribution $I(x)$ for fixed Y is depicted in Fig. 5. For perfect focusing with $W_{20} = 0$, period $p = 58$ μm, $\sin\beta = 0.4$, N.A. = 0.52, and $\lambda = 0.62$ μm, the fringe intensity is given by curve a. A height variation Δh corresponds to a focus deviation. For $\Delta h = 28.5$ μm, which corresponds to a wave-front aberration of $W_{20} = 12\lambda$ at the border of the pupil of objective MO, $I(x)$ is given by curve b. It can be seen that curve b is displaced laterally with virtually no loss of fringe modulation. This holds even for defocus distances larger than the primary range $H_p = p/(2\sin\beta) \approx 74$ μm and corresponds to the desired effect of fringe displacement that is due to height variations. For monochromatic light and stronger defocusing, self-imaging effects arise, and the shape of the fringe intensity can be

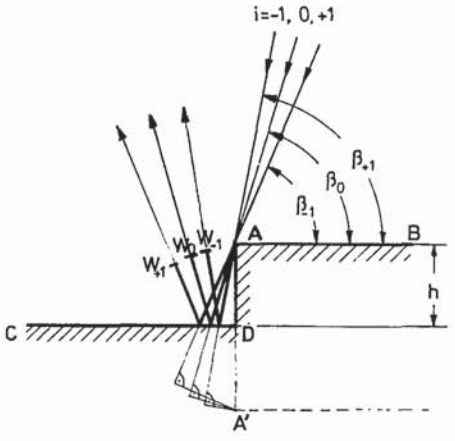

Fig. 4. Wave fronts of the underlying three-beam interference on a step CDAB on the surface. The path differences introduced by the step are $2h\cos\beta_i$, $i = -1, 0, +1$.

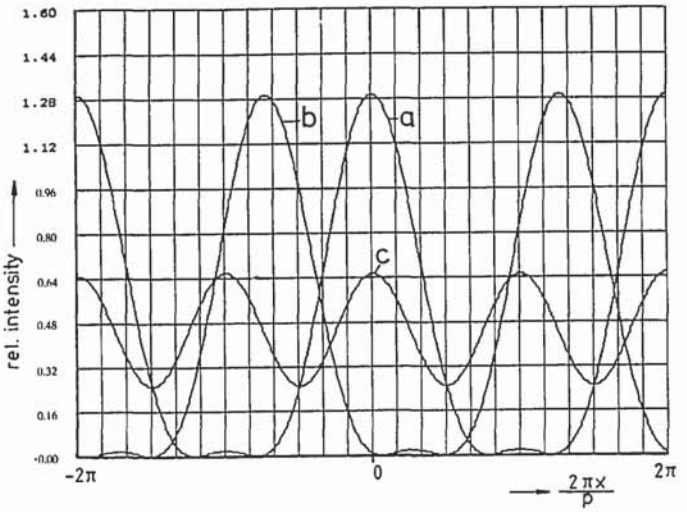

Fig. 5. Intensity distribution of the filtered and projected grating lines [Eq. (9)]: a, surface in focus; b, object height $\Delta h = 28.5$ μm, which corresponds to a focus deviation of $W_{20} = 12\lambda$; c, very strong defocusing (practically irrelevant in applications). Only the second harmonic in Eq. (9) is effective. This corresponds to the Talbot effect for on-axis, free-space propagation of gratings.

deformed [for extremely high defocusing, $W_{20} = 3308\lambda$, the fundamental component with period p in the intensity distribution can disappear, and only the second-order harmonics with period $p/2$ are left (Fig. 5, curve c)]. However, for practical applications with partially coherent illumination, this effect is not relevant. In practice, the range of good visibility of the fringes is very much larger than the vertical resolution, as specified by the Rayleigh range $H_r = \lambda/\text{N.A.}^2 \approx 2.3$ μm.

The image is digitized and stored in a 512 × 512 × 8 bit frame as the intensity signal $J(x, y)$, which is given by the optical intensity $I(x, y)$. From the argument of the intensity function [Eq. (9)], a fringe displacement Δx is linearly related to a height variation Δh:

$$\Delta h = \frac{\Delta x}{2 \sin \beta}, \qquad \sin \beta = \frac{d}{f_{\text{MO}}}, \tag{11}$$

where f_{MO} is the focal length of the MO and d is the lateral shift of the spectrum. One of our phase algorithms is a spatially integrating synchronous detection, which is related to those of Refs. 6 and 7. It calculates the real discrete Fourier coefficients $a_0(Y, x_i)$, $a_1(Y, x_i)$, and $b_1(Y, x_i)$ for each sampling point i of each column; Y = constant. Thus a sinusoid $J_f(x_i, Y)$ is fitted to one period of the preprocessed intensity signal $J(x_i, Y)$, which is sampled in the image acquisition board:

$$J_f(x_i, Y) = a(x_i, Y) + a_1(x_i, Y)\cos\left(2\pi \frac{i}{N}\right) + b_1(x_i, Y)\sin\left(2\pi \frac{i}{N}\right), \tag{12}$$

$$a_1(x_i, Y) = \frac{N}{2} \sum_{j=i}^{i+N-1} J(x_j, Y)\cos(2\pi j/N), \tag{13}$$

$$b_1(x_i, Y) = \frac{N}{2} \sum_{j=i}^{i+N-1} J(x_j, Y_j)\sin(2\pi j/N), \tag{14}$$

$$a(x_i, Y) = N \sum_{j=i}^{i+N-1} J(x_j, Y), \tag{15}$$

$$h(x_i, Y) = \frac{p}{4\pi \sin \beta} \arctan \frac{b_1(x_i, Y)}{a_1(x_i, Y)}, \tag{16a}$$

where $h(x_i, Y)$ is the topography height and N is the pixel number per period. Owing to the spatial filtering of the grating spectrum, the fringe intensity [Eq. (9)] is composed by the cosine of the fundamental order and of a second order only. Therefore we can alternatively apply a 90°-phase four-step algorithm by shifting the grating in plane G laterally:

$$I_i = I_0[1 + s^2 + 4s \cos(\alpha + \Theta_i) + 2s^2 \cos(2\alpha + 2\Theta_i)], \quad \Theta_i = 0, \pi/2, \pi, 2\pi/3,$$

$$h(x_i, y_i) = \frac{p}{4\pi \sin \beta} \arctan \frac{I_4 - I_2}{I_1 - I_3}. \tag{16b}$$

The terms with $\cos(2\alpha + 2\Theta_i)$ cancel in Eqs. (16b). Thus the algorithm is insensitive to the second-order intensity contributions.

4. Optical and Digital Preprocessing for Very Rough Surfaces

Figure 6 shows a photograph of a monitor display of a very rough surface of sheet metal illuminated with the grating lines. For topometry, the areas with low intensities are difficult for phase evaluation. These black holes result from locations on the surface where the light, which is scattered on inclined surface elements or on elements with microroughness within the resolution spot, can no longer pass entrance pupil EP and is lost. We call this effect scatter vignetting.

Fig. 6. Photograph of a monitor display with deformed and disrupted grating lines that appear when the deep-drawing sheet steel surface of Fig. 11 is measured.

It has no serious consequences in conventional imaging. However, when the topography is measured, spikes or clusters of spikes can be introduced and distributed over the topography by unwrapping procedures. Furthermore, noise worsens the situation. Temporal noises of different camera frames are statistically independent and can be suppressed if they are averaged over several intensity frames. Spatial noise is more difficult to suppress and can be introduced as additive noise n_a and multiplicative noise n_m:

$$J_n(x) = J(x)n_m(x) + n_a(x), \tag{17}$$

where $J(x)$ is the intensity signal stored in the frame grabber that is due to the optical intensity $I(x)$, a constant conversion factor that is omitted. Additive noise is modeled as a constant term c_a, which describes mainly stray light and an offset in the signal transfer, and a random variable $r_a(x)$, which describes the spatial fluctuations:

$$n_a(x) = \langle J\rangle[c_a + r_a(x)]; \quad 0 < c_a \ll 1, \quad |r_a|_{\max} < c_a,$$
$$E\{r_a\} = 0, \quad E\{r_a^2\} = \sigma_a^2, \tag{18}$$

where $E\{\ldots\}$ denotes the expectation value[12] and $\langle J\rangle$ denotes the mean intensity. Multiplicative noise is described by the random variable r_m:

$$n_m(x) = 1 + r_m(x); \quad r_m \ll 1, \quad E\{r_m\} = 0, \quad E\{r_m^2\} = \sigma_m^2. \tag{19}$$

A. Smoothing

Smoothing the intensity field is widely used, with the drawback of loss of resolution. We apply a smoothing operator optionally as a convolution operator of width m:

$$J_s(X, y) = \frac{1}{m}\sum_{u=-k}^{+k} J(X, y - u);$$
$$k = (m - 1)/2, \qquad m = 3, 5, 7, \ldots. \tag{20}$$

B. Subtraction of a π-Phase-Shifted Intensity Field

The second-order contribution of the intensity [Eq. (9)] can be eliminated by subtraction of a π-shifted intensity, $I_\pi(x_i, y_i)$, which is produced when the grating is shifted laterally by half of the grating period. With $\alpha = 2\pi[x - 2h(x)\sin\beta)/p$, the normalized difference of the unshifted intensity signal $J_n(x_i)$ and the π-shifted signal $J_{\pi n}(x_i)$ is

$$J_{\text{sub}} = [1 + 2s^2 + 4s\cos(\alpha) + 2s^2\cos(2\alpha)]n_m + n_a$$
$$- [1 + 2s^2 - 4s\cos(\alpha) + 2s^2\cos(2\alpha)]n_m - n_a,$$
$$J_{\text{sub}}(x) = 8s\cos(\alpha)n_m(x). \tag{21}$$

The intensity signal $J_{\text{sub}}(x)$ is now a sinusoid of the fundamental frequency. Additive time-independent noise is eliminated by the π-shifting-and-subtraction process. However, multiplicative noise $n_m(x)$, including variations of the illuminating intensity across the object field, and variations of surface reflexivity are not compensated.

In the Fourier transform $\tilde{J}(f_x)$ of $J_{\text{sub}}(x)$ the noise spectrum $\tilde{r}_m(f_x)$ is convolved over the even-impulse pair $\text{II}(f_x p)$ with the fundamental frequency $f_o = 1/p$ of the projected grating. The signal-to-noise ratio S is thus given by

$$S^2 = \frac{1}{2\sigma_m^2}. \tag{22}$$

C. π-Shift-and-Division Process

We empirically found that in the topographies of very rough surfaces, a division by a π-shifted second frame of the intensity field results in fewer spikes and fewer unwrapping errors. The idea that led us to investigate the division as a preprocessing step was to find a means to compensate for the multiplicative noise. With the direct detection process, according to Eqs. (12)–(16a), or with the π-shifting-and-subtraction process, spatially low-frequency multiplicative noise results in errors in the measured height field. We demonstrate this by a numerical simulation of an artificially generated stair function [Fig. 7(a)] and an illumination function [Fig. 7(b)] that simulates a linearly increasing intensity of the projected grating in the x direction. Figure 7(c) shows an erroneous waviness of the resulting height field. The period of the waviness is the same as the period of the projected fringes. This serious error can be suppressed by the use of the π-shift-and-division process:

$$J_{\text{div}}(x) = \frac{\{1 + 2s\gamma\cos[\alpha(x)]\}^2 n_m(x) + c_a + r_a(x)}{\{1 - 2s\gamma\cos[\alpha(x)]\}^2 n_m(x) + c_a + r_a(x)}. \tag{23}$$

The factor γ has been introduced because of a reduction in the visibility that is due to residual aberrations and coherence effects. For small additive noise n_a we approximate

$$\frac{n_a(x)}{I_0 n_m(x)} = v(x) \approx c_a + r_a(x) - c_a r_m(x), \tag{24}$$

$$J_{\text{div}}(x) = \frac{1 + v(x) + 4s\gamma\cos\alpha(x) + 4s^2\gamma^2\cos^2\alpha(x)}{1 + v(x) - 4s\gamma\cos\alpha(x) + 4s^2\gamma^2\cos^2\alpha(x)}. \tag{25}$$

We note that the contribution of multiplicative noise in the term $c_a r_m(x)$ of Eq. (24) leads to a second-order effect. For $n_a = c_a = 0$ it is completely eliminated. A graph of the intensity signal J_{div} over α is plotted in Fig. 8 for $r_a = r_m = 0$, $c_a = 0.05$, and some values of γ. For $c_a = 0$ and $\gamma > 0.785$, $J_{\text{div}}(\alpha)$ can exhibit poles. However, with increasing c_a or decreasing γ, the variation of J_{div} is damped to a nearly sinusoidal distribution to which the phase algorithm can be readily applied. To investigate the signal-to-noise ratio S, we find, by a polynomial division and by

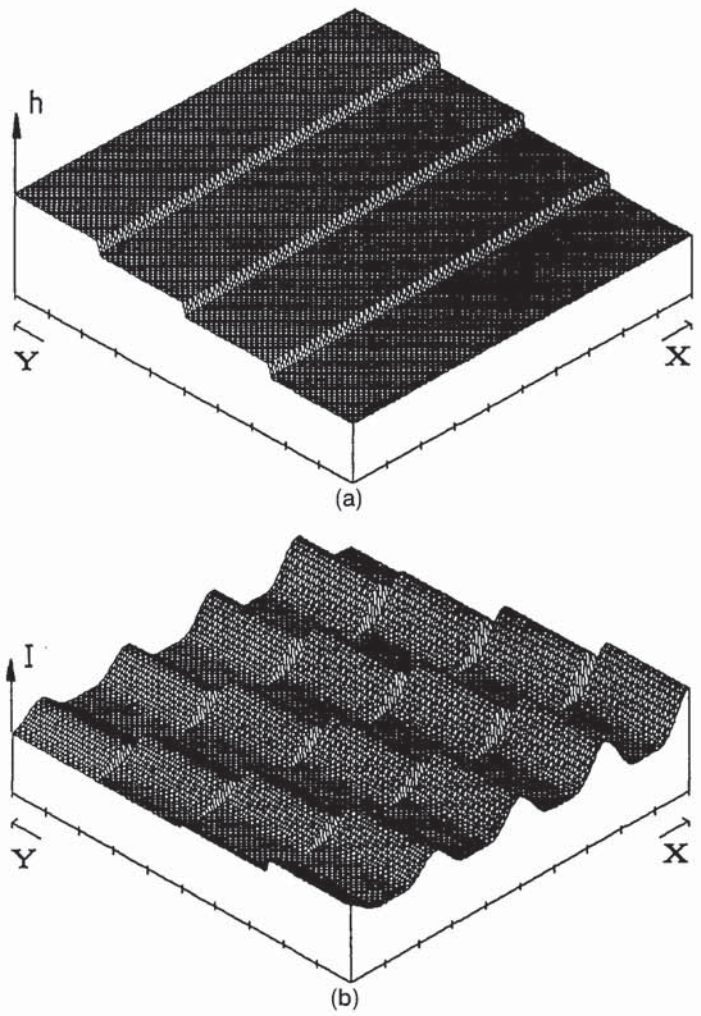

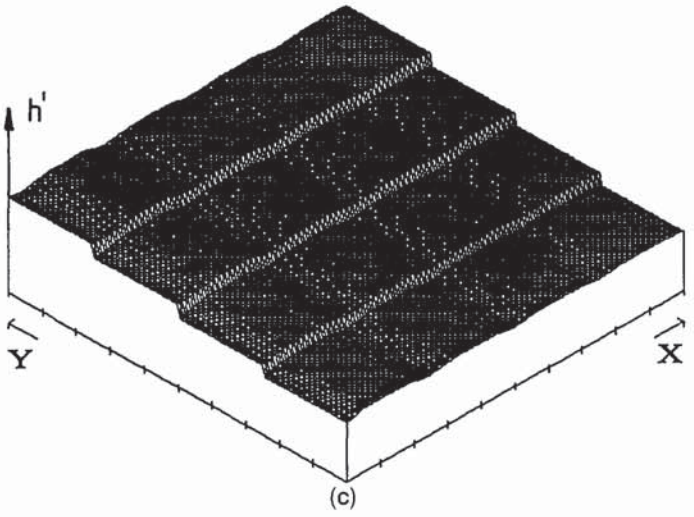

Fig. 7. Simulation of the topography of a staircase object under illumination with an inhomogeneous intensity distribution (low-frequency multiplicative noise) to show erroneous height modulation in the form of waves parallel to the grating lines if the direct process or the π-shift-and-subtraction process is used: (a) simulation of the object height field $h(x, y)$, (b) calculated intensity distribution $I(x, y)$ according Eqs. (16) with a linearly increasing multiplicative factor in the x direction, (c) topography $h(x, y)$ calculated from (b) with the resulting erroneous waviness of the same period as the projected grating. If the π-shift-and-division process is used, no waviness in the topography occurs.

neglecting higher harmonics terms,

$$J_{\text{div}}(\alpha) = 1 + 8s\gamma \cos(\alpha)[1 - c_a - r_a(\alpha) + c_a r_m(\alpha)] + \cdots . \tag{26}$$

In the Fourier transform $\tilde{J}(f_x)$ of Eq. (26) the noise spectra $\tilde{r}_a(f_x)$ and $\tilde{r}_m(f_x)$ are again convolved over the even-impulse pair $\text{II}(f_x p)$ with the fundamental frequency $f_c = 1/p$ of the projected grating. But, in contrast to the subtraction process, the spectrum of the multiplicative noise is multiplied with the small number c_a and vanishes for $c_a = 0$:

$$\tilde{J}(f_x) = \delta(f_x) + \frac{1}{p} 8(1 - c_a)s\gamma \text{II}(f_x p) + \frac{1}{p} 8s\gamma c_a \tilde{r}_m(f_x) * \text{II}(f_x p) - \frac{1}{p} 8s\gamma \tilde{r}_a(f_x) * \text{II}(f_x p). \tag{27}$$

The second term in Eq. (27) is the signal term, whereas the third and the fourth terms are the noise terms. Thus we define a signal-to-noise ratio, S_{div}, as

$$S_{\text{div}}{}^2 = \frac{(1 - c_a)^2}{2(c_a{}^2 \sigma_m{}^2 + \sigma_a{}^2)}, \tag{28}$$

where σ_m and σ_a are the standard deviations of the multiplicative and the additive noises, respectively. For cases in which multiplicative noise, including variations of the illumination and of surface reflexivity across the object field, is critical, the π-shift-and-division process is advantageous. The number of spikes on critical surfaces is smaller than that obtained by the other processes.

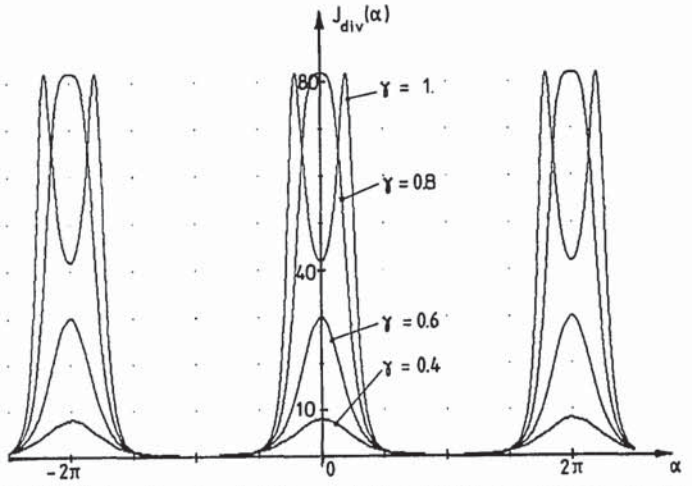

Fig. 8. Intensity signal of the π-shift-and-division process, $J_{\text{div}}(x)$ [Eq. (25)], for a plane surface: $c_a = 0.05$, $r_m = r_a = 0$, and $0.4 < \gamma < 1.0$ (as a parameter).

D. Subtraction of a Reference Topography to Compensate for Shape Deviations

Because of residual optical aberrations, even for a perfect plane, the images of the projected grating lines deviate from perfect straight lines. Therefore the topography, even of a perfect plane, can be deformed. To compensate for this error, we subtract a reference topography $h_{\text{ref}}(x_i, y_i)$, taken from a good plane mirror under the same conditions, from each object topography $h'(x_i, y_i)$:

$$h(x_i, y_i) = h'(x_i, y_i) - h_{\text{ref}}(x_i, y_i). \tag{29}$$

E. Averaging over Two Opposite Projection Directions

Shadowed parts of the surface or parts with large local slopes or discontinuities may not modulate the projected intensity of Eq. (9). Information on the height is then lost for the particular direction of projection, and noise dominates. To overcome this problem, we average the height field $h_{\text{I}}(x_i, y_i)$ from the first direction with the unshadowed height field $h_{\text{II}}(x_i, y_i)$ of a second frame under an opposite angle $\beta_{\text{II}} = -\beta_{\text{I}}$. The spectrum of the grating is shifted to the opposite border of pupil EP (Fig. 1) by a shift of O1. The contribution of each topography to the final topography $h(x_i, y_i)$ can be weighted by the mean intensities of Eq. (5), $a_{\text{I}}(x_i, y_i)$, $a_{\text{I}\pi}(x_i, y_i)$, $a_{\text{II}}(x_i, y_i)$, and $a_{\text{II}\pi}(x_i, y_i)$, where the subscripts I and II stand for the two directions and π stands for the π-shifted frames:

$$h(x_i, y_i) = \frac{[a_{\text{I}}(x_i, y_i) + a_{\text{I}\pi}(x_i, y_i)]h_{\text{I}}(x_i, y_i) + [a_{\text{II}}(x_i, y_i) + a_{\text{II}\pi}(x_i, y_i)]h_{\text{II}}(x_i, y_i)}{a_{\text{I}}(x_i, y_i) + a_{\text{I}\pi}(x_i, y_i) + a_{\text{II}}(x_i, y_i) + a_{\text{II}\pi}(x_i, y_i)}. \tag{30}$$

In critical applications such as those of Fig. 6, the height of the direction that is unshadowed enters Eq. (30) with preference, because in these locations the corresponding weighting factor a is greater. The process given by Eq. (30) can be generalized in a straightforward manner to more than two directions.

5. Resolution and Measuring Range

Important characteristics of a measuring method are vertical and lateral resolutions. Vertical resolution δ_h can be introduced as the standard deviation or the rms value of the spurious height topography, which is due to noise, of a plane surface with negligible roughness. For measuring methods for which the signal-to-noise ratio is low and the pixel distance Δx_p (reduced to the object plane) is greater than the Rayleigh distance Δx_r of diffraction-limited image formation, lateral resolution is limited by the width of patches of noise of such a noise topography. Small lateral details can be restored if and only if they are broader than the noise patches, e.g., if they contain substantially longer spatial wavelengths. This must be true because in this case the noise contributions can be effectively suppressed by low-pass filtering in postprocessing, and details of the object can be enhanced. This is the case in most of our applications. Thus a unified treatment of vertical and lateral resolutions can be based on the autocorrelation function of the noise topography: vertical resolution is the square root of $R_{hh}(\Delta = 0)$ of the zero-mean noise topography and the autocorrelation width in a suitable definition and with suitable conventions, as filtering of the topography is a measure of lateral resolution.

A typical experimental example is the noise topography of a high-quality plane mirror [Fig. 9(a)]. The raw topography is high-pass filtered with a cutoff wavelength of $L_c = L = 96$ μm, where L is the length of the object field, which is much greater than the lateral resolution expected. Figure 9(b) shows a quadrant of the (noncircular) autocorrelation of the noise topography. The vertical resolution is $\delta_h = \sigma_h = 7.1$ nm. The widths of the autocorrelation, which are measured as e^{-1} − width, are $w_y = 1.8$ μm and $w_x = 3.1$ μm. In contrast, the Rayleigh distance of two-point resolution, $\Delta x_r = 1.22\lambda/(2\ \text{N.A.})$, would be 0.39 μm with N.A. = 0.85 and $\lambda = 0.55$ μm. This value is of little significance because the aperture is only partially filled, and a smoothing operation is implicitly involved in the phase algorithms [Eqs. (12)–(16a)].

The fringe phase deviations that are due to noise on a perfect surface are $\ll \pi/2$. To find analytical expressions for vertical resolution, we approximate h_i of Eq. (16a) by

$$h_i = \frac{p}{4\pi \sin \beta}\left(\frac{b_i}{a_i}\right). \tag{31}$$

Assuming that J_i and h_i are wide-sense stationary and ergodic processes,[12] the autocorrelation $R_{hh}(t)$ of the noise topography can then be estimated as

$$R_{hh}(t) = \frac{1}{N_t}\sum_{i=1}^{N_t} h_i h_{i+t} = \frac{p^2}{16\pi^2 \sin^2 \beta\, N_t}\sum_{i=1}^{N_t}\frac{b_i b_{i+t}}{a_i a_{i+t}}, \tag{32}$$

where $\langle h_i \rangle = \langle h_{i+t} \rangle = 0$ and N_t is the total number of pixels of each column. In Appendices A and B, $R_{hh}(t)$ is derived for the most important processes of this work.

A. Direct Process

We call the process of Sections 2 and 3 the direct process, in which only one direction without a π shift is used for the calculation of the topography. The resulting autocorrelation function of the noise topography is derived in Appendix A:

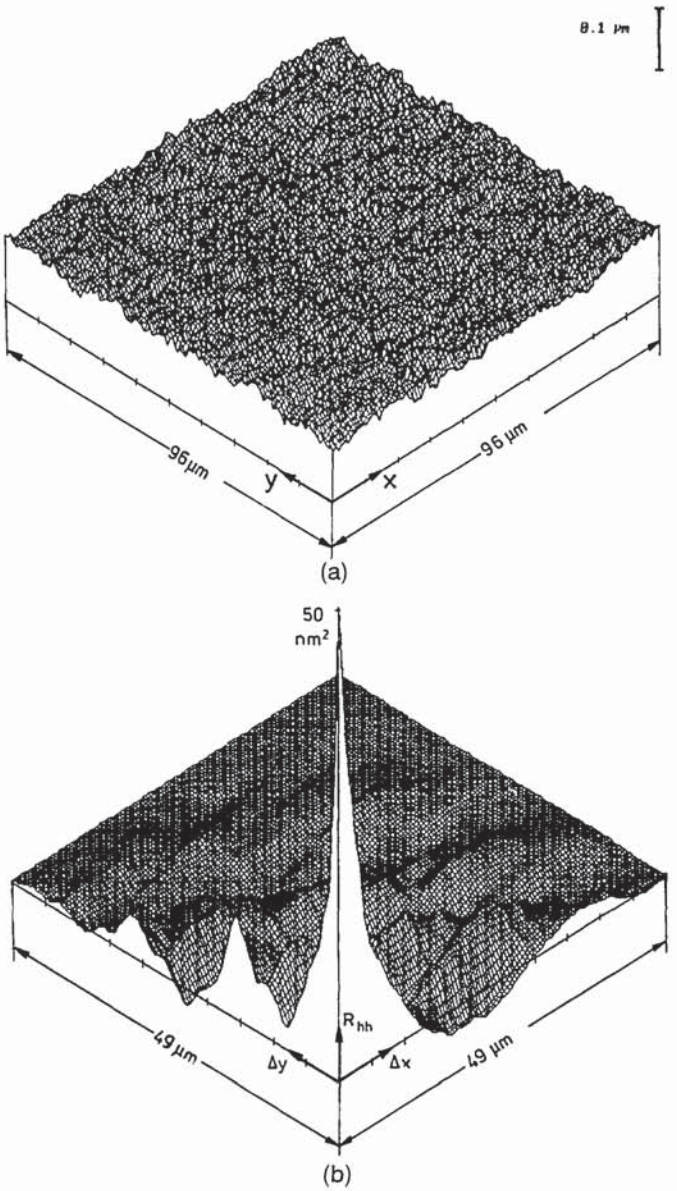

Fig. 9. Noise topography obtained, with a 50 × 0.85 microscope objective, by the π-shift-and-division process: (a) topography of a high-quality plane mirror after subtraction of a plane, fitted for a least-square deviation. (b) Autocorrelation function (ACF): vertical resolution $\delta_h = \mathrm{ACF}(0, 0)^{0.5} = 7.1$ nm; the autocorrelation widths, which are defined as e^{-1} − width, are $w_x = 3.1$ μm and $w_y = 1.8$ μm.

$$R_{hh}(t) \approx \frac{p^2}{16\ 8s^2 \sin^2 \beta\pi^2 N}\{(1 + 2s^2)^2[R_m(t) + R_a(t)] + (8s^2 + 2s^4)R_m(t)\}. \quad (33)$$

The vertical resolution δ_h is given by $R_{hh}(t = 0)$. With the signal-to-noise ratio S of the intensity signal, where ${\sigma_m}^2$ is the variance of the multiplicative noise and ${\sigma_a}^2$ is the variance of the additive noise, and

$$S^2 = \frac{8s^2}{(1 + 2s^2)({\sigma_m}^2 + {\sigma_a}^2) + (8s^2 + 4s^4){\sigma_m}^2}, \quad (34)$$

we get the final expression for the vertical resolution $\delta_{h\mathrm{dir}}$ of the direct process:

$$\delta_{h\mathrm{dir}} = \sigma_h = \frac{p}{4\pi \sin \beta S\sqrt{N}}, \quad (35)$$

where p is the period of the projected grating on the object, β is the projection angle, and N is the number of sample values within one period. S can be assessed experimentally from a trace of the intensity signal across the grating lines.

With $\Delta x_c M^{-1} N = p$, where Δx_c is the pixel separation on the CCD chip, M is the magnification of the imaging system, $M = f_{\mathrm{CCD}}/f_{\mathrm{MO}}$, L is the length of the object field, and N_{tot} is the total pixel number, Eq. (35) can be rewritten as

$$\delta_{h\mathrm{dir}} = \frac{\Delta x_c \sqrt{N} M^{-1}}{4\pi \sin \beta S} = \frac{\sqrt{N}L}{4\pi \sin \beta N_{\mathrm{tot}} S}. \quad (36)$$

B. Coherent Process

The intensity distribution of the coherent process,

$$J_j = 0.5\left[1 + K \cos\left(\frac{2\pi}{N}\, j\right)\right](1 + r_m) + c_a + r_a, \quad (37)$$

can be realized by coherent interferometric fringes, where K is the visibility of the fringes. In this process, according to Eq. (37), the intensity signal assumes its most simple form. From the autocorrelation, which is derived in Appendix B, we get the vertical resolution $\delta_{h\mathrm{coh}}$:

$$\delta_{h\mathrm{coh}} = \frac{p}{4\pi \sin \beta \sqrt{N} S}. \quad (38)$$

The signal-to-noise ratio S in this case is given by

$$S^2 = K^2/[2({\sigma_m}^2 + {\sigma_a}^2) + K^2{\sigma_m}^2/2]^{-1}. \quad (39)$$

C. Process with π Shift and Subtraction

From Subsection 4.B, following the same steps as above, we find

$$R_{hh}(t) = \frac{p^2{\sigma_m}^2}{16\pi^2 \sin^2 \beta N} \cos(2t). \quad (40)$$

With signal-to-noise ratio S from Eq. (21), $S = 1/(2{\sigma_m}^2)$, we get, from Eq. (40),

$$\delta_{h\mathrm{sub}} = \frac{p}{4\sqrt{2}\pi \sin \beta \sqrt{N} S} = \frac{\sqrt{N}L}{4\sqrt{2}\pi \sin \beta N_t S}, \quad (41)$$

where L is the length of the object field and N_t is the total number of pixels of a column.

D. Process of π Shift and Division

For fringe projection with π shift and division, we find, for the vertical resolution,

$$\delta_{h\mathrm{div}} = \frac{p}{4\sqrt{2}\pi \sin \beta S\sqrt{N}} = \frac{\sqrt{N}L}{4\sqrt{2}\pi \sin \beta N_t S}, \quad (42)$$

with the signal-to-noise ratio defined according to Eq. (28):

$$S_{\text{div}}^2 = S_{\text{dir}}^2 = \frac{(1 - c_a)^2}{2(c_a^2\sigma_m^2 + \sigma_a^2)} \approx \frac{1}{2\sigma_a^2}. \quad (43)$$

Multiplicative noise enters as a second-order quantity. In practice, the variance of the additive noise σ_a^2 enters the square of the signal-to-noise ratio S instead of the variance of multiplicative noise σ_m^2 in the case of the π-shift-and-subtraction process.

E. Measuring Range, Dynamic Range, and Limitation of Resolution by Diffraction

The measuring range and the dynamic range are important characteristics of a measuring technique. For sufficiently smooth surfaces for which distinct and nonclosed grating lines can be detected on the surface, the technique of phase unwrapping can be employed. As in the case of phase-measuring interferometry, the total measuring range H_t is m times the primary unambiguous range or contouring interval H_p:

$$H_t = mH_p, \qquad H_p = \frac{p}{2 \sin \beta}. \quad (44)$$

where m is the unwrapping order and H_p is the height of a step that corresponds to a fringe displacement of one period. We can define the dynamic range as $B = H_t/\delta_h$, where δ_h is the vertical resolution. For the direct and the coherent processes we get, from Eqs. (35) and (38),

$$B_{\substack{\text{dir} \\ \text{coh}}} = 2m\sqrt{N}\pi S. \quad (45)$$

For the π-shift-and-division and the π-shift-and-subtraction processes we get, from Eqs. (41) and (42),

$$B_{\substack{\text{div} \\ \text{sub}}} = 2\sqrt{2}m\pi S\sqrt{N}. \quad (46)$$

It is important to note that, in every case, the dynamic range B is independent of the grating period p and of the projection angle β and increases with the square root of the number of pixel per fringe period N.

For relatively small object fields, resolution can be limited by the fact that the grating must be resolved. For a diffraction-limited system with a degree of coherence close to 1, not limited by the pixel distance, and for signal-to-noise ratio $S \gg 1$, the minimal resolved period is $p_{\min} = (2\lambda f_{\text{MO}})/D_c$, where $D_c = D - 2d$; Fig. 2 is the free aperture of the fringe projection. For the direct process, [Eq. (35)], the diffraction-limited height resolution δ_h is thus

$$\delta_{h\min} = \frac{\lambda f_{\text{MO}}}{2\pi\sqrt{N} \sin \beta S D_c} = \frac{\lambda}{4\pi\sqrt{N} \sin \beta (\text{N.A.} - \sin \beta) S}, \quad (47)$$

where N.A. $= D/2f_{\text{MO}}$ is the numerical aperture of the objective. Equation (47) corresponds to the single-aperture FPM. Of course, Eq. (47) can be adapted to the case of conventional fringe projection with separated projection and imaging arms. In this case $D_c = D$, and we get

$$\delta_{h\min} = \frac{\lambda}{4\pi\sqrt{N} \sin \beta \text{ N.A. } S}. \quad (48)$$

For single-aperture FPM we find from Eq. (47) that for a 100 × 0.95 objective, even for a moderate signal-to-noise ratio of $S \approx 30$, $\lambda \approx 0.5$ μm, $N = 12$, and $\sin \beta = 0.5$, the height resolution can be less than 1 nm.

6. Applications and Aspects for the Future

The performance of our present FPM can be demonstrated by selected topographies. We used the π-shift-and-division process as in Subsection 4.C and averaged over two opposite directions as in Subsection 4.E. The following topographies have been produced with a microscope (Zeiss Axiovert). The basic system was modified to fit our fringe projection and some additional modifications.

Figure 10 is the topography of the largest groove of a PTB calibration standard (i.e., a calibration standard of the Physikalische Technische Bundesanstalt, PTB, Braunschweig, Germany). The grooves are lapped into a glass block. The certified depth is 9.00 ± 0.05 μm in the middle of the groove. We used a 10 × 0.3 objective, and the grating period was 25 μm. The measured peak-to-valley value was PV = 9.08 μm, which corresponds to the depth of the groove. The theoretical height resolution, according to Eq. (35), is $\delta_h \simeq 80$ nm when a signal-to-noise ratio of $S = 25$ is assumed. Figure 11(a) shows the topography of the oil-bearing structure on deep-drawing sheet steel. The object field is 531 μm ×

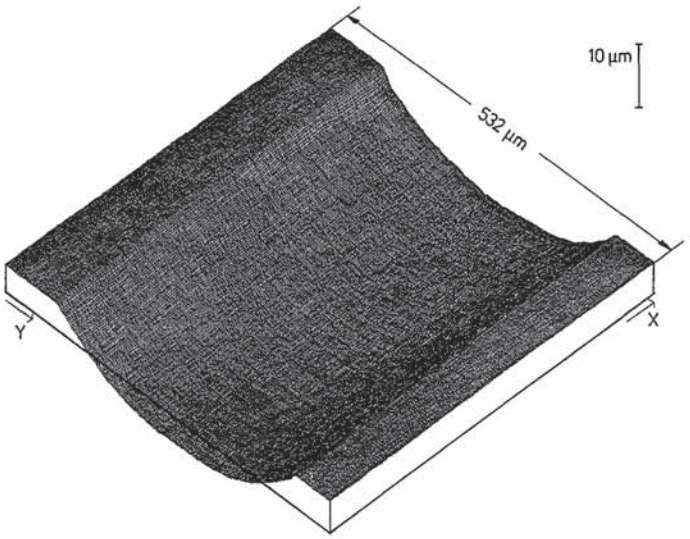

Fig. 10. Groove 6 of a PTB calibration standard. The certified depth is 9.00 ± 0.05 μm; the peak-to-valley value over the whole topography is evaluated as 9.08 μm.

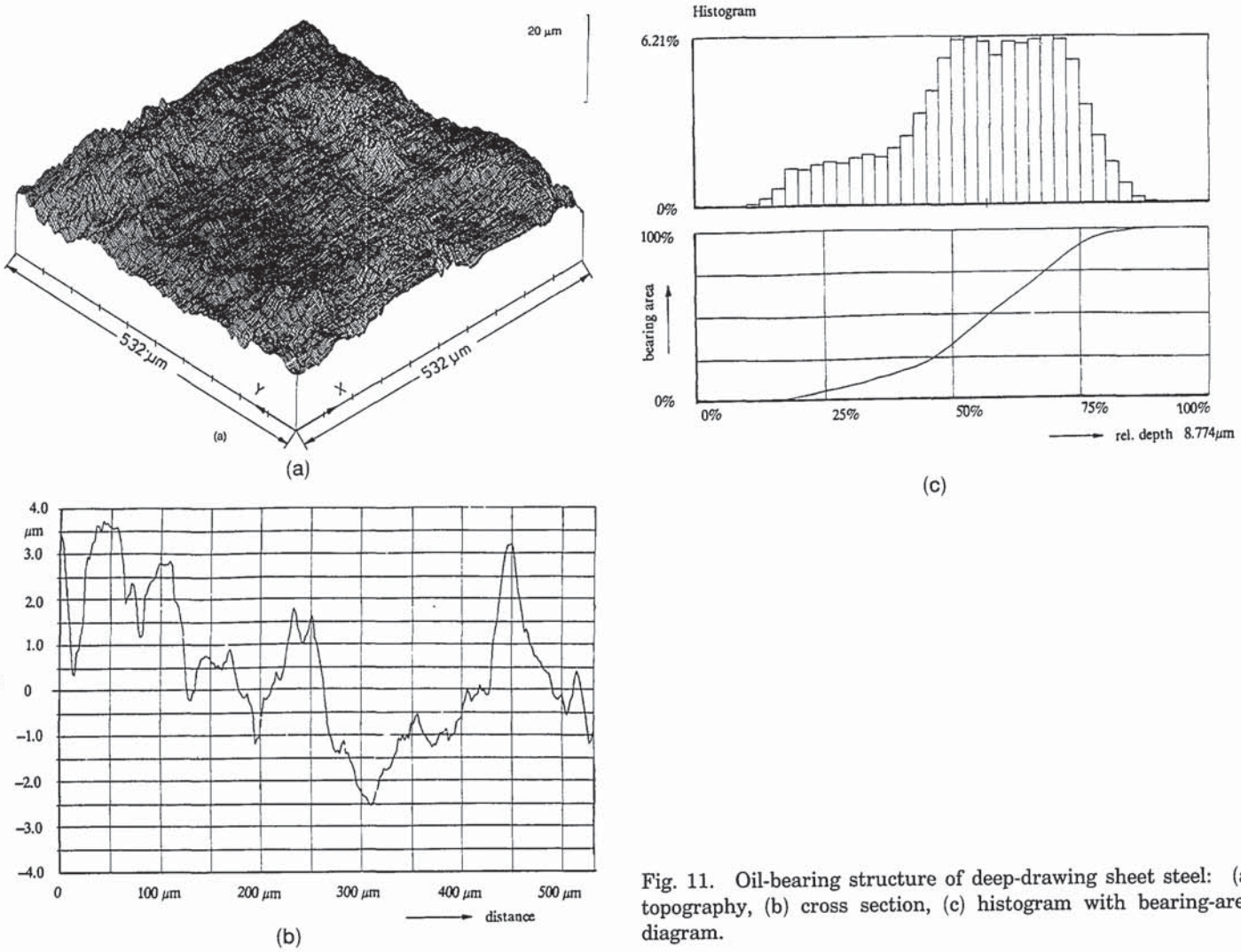

Fig. 11. Oil-bearing structure of deep-drawing sheet steel: (a) topography, (b) cross section, (c) histogram with bearing-area diagram.

531 μm. The investigation of such structures is important in current automobile engineering. The roughness is evaluated as follows: PV = 8.77 μm, rms roughness R_q = 1.38 μm, and arithmetic average roughness R_a = 1.12 μm. Figure 11(b) is a cross section in the y direction. In Fig. 11(c) the histogram with non-Gaussian probability density is depicted. The skewness of the density is $\gamma_a = +0.6$; positive skewness indicates a bearing structure of narrow and steep summits and broader valleys that act as oil reservoirs. The topography of Fig. 12 is a measurement of a detail of a microlithographic processing step. A 50 × 0.85 objective was used for this task. The object field is 155 μm × 155 μm. Lateral and vertical resolutions as estimated from a corresponding noise topography are $\delta_y \approx 1.2$ μm, $\delta_x \approx 3.4$ μm, and $\delta_h \approx 6$ nm.

FPM is a powerful tool for microstructure analysis. Our symmetric single-aperture FPM is much more robust and tolerant to roughness and discontinuities of the surface than interference microscopy. Compared with confocal microscopy or coherence scanning, FPM results in lower costs for the instrumentation and faster processing. Object fields realized so far vary between 2500 μm × 2500 μm and 100 μm × 100 μm. Vertical resolution can be less than 1 nm; so far we have reached a few nanometers. Optical filtering of the grating spectrum as described in Section 2 completely removes harmonics of the fringe intensity that are higher than second order. The described preprocessing methods render the remaining second order in Eq. (9) harmless. The four-interferogram phase-stepping method is shown to be

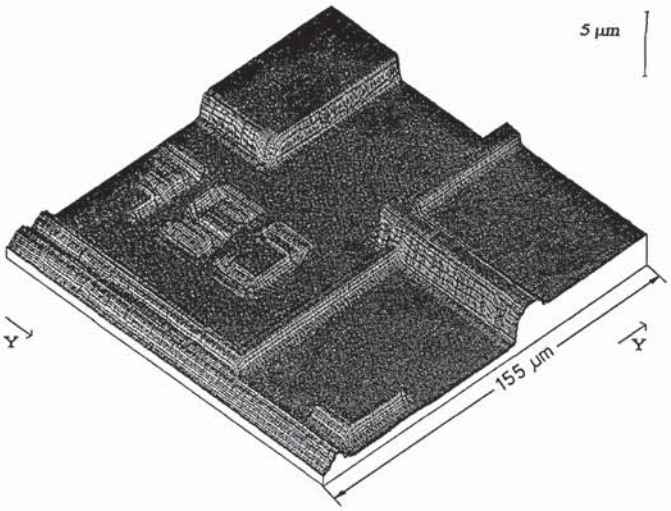

Fig. 12. Microchip topography measured with a 50 × 0.85 objective.

insensitive to these second-order harmonics. We use this pixel-oriented, temporal carrier method [Eq. (16b)] as an alternative to the spatial carrier method [Eqs. (12)–(16a)] when high accuracy and freedom of systematic errors in the height field of moderately structured objects are needed. For relatively rough surfaces with large local slopes and discontinuities, we obtain our best results by applying the spatial carrier method and the processes of π shifting, division, and averaging from opposite directions. For fast processing of moderately rough objects, the direct process can be used. It follows from the analysis of Sections 4 and 5 that lateral and vertical resolutions, freedom from spikes, and systematic errors can be effectively improved by the use of cameras with larger pixel numbers and improved dynamic range of the detected signal.

Appendix A: Autocorrelation of the Noise Topography of the Direct Process

For the direct process, the intensity signal J_j is given by Eqs. (9) and (17):

$$J_j = (1 + 2s\cos\alpha_j)^2(1 + r_{mj}) + \langle J\rangle(c_a + r_{aj}); \qquad \langle J\rangle = 1 + 2s^2. \quad \text{(A1)}$$

Noise has been introduced from Eqs. (17)–(19) and $\alpha_j = 2\pi j/N$, with defocusing neglected. From Eqs. (13) and (14) the imaginary part b_i of the first-order Fourier coefficient is

$$b_i = \sum_{j=i}^{i+N-1} [(1 + 2s^2)(1 + c_a)\sin\alpha_j + (4s\cos\alpha_j + 2s^2\cos 2\alpha_j)\sin\alpha_j + (1 + 2s^2)(r_{mj} + r_{aj})\sin\alpha_j + (4s\cos\alpha_j + 2s^2\cos 2\alpha_j)r_{mj}\sin\alpha_j]. \quad \text{(A2)}$$

When the summation and the orthogonality relations,

$$\sum_{j=1}^{N}\sin\left(\frac{2\pi kj}{N}\right) = \sum_{j=1}^{N}\cos\left(\frac{2\pi lj}{N}\right) = \sum_{j=1}^{N}\sin\left(\frac{2\pi kj}{N}\right)\cos\left(\frac{2\pi lj}{N}\right) = 0 \qquad k, l = \pm 1, \pm 2, \ldots,$$

$$\sum_{j=1}^{N}\cos\left(\frac{2\pi kj}{N}\right)\cos\left(\frac{2\pi lj}{N}\right) = \sum_{j=1}^{N}\sin\left(\frac{2\pi kj}{N}\right)\sin\left(\frac{2\pi lj}{N}\right) = \frac{N}{2}\delta_{kl}, \quad \text{(A3)}$$

are used, the real part a_i reduces to

$$a_i \approx \sum_{j=i}^{i+N-1} 4s(\cos\alpha_j)^2 = 4sN\frac{1}{2}, \quad \text{(A4)}$$

where δ_{kl} is the Kronecker δ. The terms 1 and 2 in Eq. (A2) vanish under the summation over one period, which leads to

$$\frac{b_ib_{i+t}}{a_ia_{i+t}} \approx \frac{1}{4s^2N^2}\sum_{j1=i}^{i+N-1}\sum_{j2=i+t}^{i+t+N-1}\{[(1 + 2s^2)^2 \times (r_{mj1}r_{mj2} + r_{aj1}r_{aj2})]\sin\alpha_{j1}\sin\alpha_{j2} + 16s^2r_{mj1}r_{mj2}\cos\alpha_{j1}\sin\alpha_{j1}\cos\alpha_{j2}\sin\alpha_{j2} + 4s^4r_{mj1}r_{mj2}\cos 2\alpha_{j1}\sin\alpha_{j1}\sin\alpha_{j2}\cos 2\alpha_{j2}\}. \quad \text{(A5)}$$

The random variables r_a and r_m are independent of each other and of the sinusoidal variations. Therefore in approximation (A5) only those terms that do not lead to cross terms in r_m and r_a or sin and cos are retained. When approximation (A5) is inserted into Eq. (32) and averaging over i is performed, the autocorrelation is

$$R_{hh}(t) \approx \frac{p^2}{64s^2\sin^2\beta\pi^2N^2N_t}\sum_{j1=1}^{N}\sum_{j2=t}^{t+N}N_t\{(1 + 2s^2)^2 \times [R_m(t) + R_a(t)]\sin\alpha_{j1}\sin\alpha_{j2}\delta_{j1j2} + 16s^2R_m(t)\sin\alpha_{j1}\sin\alpha_{j2}\cos\alpha_{j1}\cos\alpha_{j2}\delta_{j1j2} + 4s^4R_m(t)\sin\alpha_{j1}\sin\alpha_{j2}\cos 2\alpha_{j1}\cos 2\alpha_{j2}\delta_{j1j2}\}, \quad \text{(A6)}$$

where R_a and R_m are the autocorrelation functions of the additive and multiplicative noise. Assuming that the period of the cos function is much larger than the width of the autocorrelation of the multiplicative and additive noise, we get

$$R_{hh} \approx \frac{p^2}{64s^2\sin^2\beta\pi^2N^2}\left\{(1 + 2s^2)^2 \times \left[R_m\left(\frac{2\pi t}{N}\right) + 4R_a\left(\frac{2\pi t}{N}\right)\right]\sum_{j=1}^{N}(\sin\alpha_j)^2 + 16s^2R_m\left(\frac{2\pi t}{N}\right)\sum_{j=1}^{N}(\sin\alpha_j)^2(\cos\alpha_j)^2 + 4s^4R_m\left(\frac{2\pi t}{N}\right)\sum_{j=1}^{N}(\sin\alpha_j)^2(\cos 2\alpha_j)^2\right\}, \quad \text{(A7)}$$

or

$$R_{hh}(t) \approx \frac{p^2}{64s^2\sin^2\beta\pi^2N} \times \left\{(1 + 2s^2)^2\left[R_m\left(\frac{2\pi t}{N}\right) + R_a\left(\frac{2\pi t}{N}\right)\right]\frac{1}{2} + 4s^2R_m\left(\frac{2\pi t}{N}\right) + s^4R_m\left(\frac{2\pi t}{N}\right)\right\}. \quad \text{(A8)}$$

Appendix B. Autocorrelation of the Noise Topography of the Coherent Process

From Eq. (37) the imaginary and the real parts b_i and a_i of the Fourier coefficient are

$$b_j = 0.5 \sum_{j=1}^{i+N-1} [(r_{mj} + r_{aj})\sin \alpha_j + r_{mj} K \cos \alpha_j \sin \alpha_j], \tag{A9}$$

$$a_i \approx 0.5 \, \Sigma \, K \cos^2 \alpha_j = \tfrac{1}{4} KN. \tag{A10}$$

Proceeding as in Appendix A, we get

$$\begin{aligned} R_{hh}(t) \approx \frac{p^2}{4K^2N^2N_t} \sum_{i=1}^{N_t} \sum_{j1=i}^{i+N-1} \sum_{j2=i+t}^{i+t+N-1} & (r_{mj1} + 2r_{aj1}) \\ & \times (r_{mj2} + r_{aj2})\sin \alpha_{j1} \sin \alpha_{j2} \\ & + K(r_{mj1} + r_{aj1}) r_{mj2} \sin \alpha_{j1} \cos \alpha_{j2} \sin \alpha_{j2} \\ & + K(r_{mj2} + r_{aj2}) r_{mj1} \sin \alpha_{j2} \cos \alpha_{j1} \sin \alpha_{j1} \\ & + K^2 r_{mj1} r_{mj2} \cos \alpha_{j1} \sin \alpha_{j1} \cos \alpha_{j2} \sin \alpha_{j2}, \end{aligned} \tag{A11}$$

which leads to

$$R_{hh}(t) \approx \frac{p^2}{8\pi^2 \sin^2 \beta N K^2} \left(R_m + R_a + \frac{1}{2} K^2 R_m \right). \tag{A12}$$

We gratefully acknowledge the availability of software, developed at the Institut für Technische Optik, Stuttgart, Germany, by M. Küchel, B. Dörband, A. Lutz, G. Schmidt, T. Ittner, L. Bai, Ch. Voland, S. Schön, H. Vetter, and others, which served us as a basis for the developments of this paper. The financial support of the Deutsche Forschungsgemeinschaft is gratefully acknowledged.

References

1. M. Takeda and K. Mutoh, "Fourier transform profilometry for the automatic measurement of 3-D object shapes," Appl. Opt. **22,** 3977–3982 (1983).
2. V. Srinivasan, H. C. Liu, and M. Halioua, "Automated phase-measuring profilometry of 3-D diffuse objects," Appl. Opt. **23,** 3105–3108 (1984).
3. S. Toyooka and Y. Iwaasa, "Automated profilometry of 3-D diffuse objects by spatial phase detection," Appl. Opt. **25,** 1630–1633 (1986).
4. M. Takeda, H. Ina, and S. Kobayashi, "Fourier-transform method of fringe-pattern analysis for computer-based topography and interferometry," J. Opt. Soc. Am. **72,** 156–160 (1982).
5. R. W. Wygant, S. P. Almeida, and O. D. D. Soares, "Surface inspection via projection interferometry," Appl. Opt. **27,** 4626–4630 (1988).
6. G. Schmalz, *Technische Oberflaechenkunde* (Springer, Berlin, 1936).
7. J. Schwider, "Advanced evaluation techniques in interferometry," in *Progress in Optics,* E. Wolf, ed. (North-Holland, Amsterdam, 1990), Vol. XXVII, pp. 271–357.
8. J. H. Bruning, D. R. Herriott, J. E. Gallagher, D. P. Rosenfeld, A. D. White, and D. J. Brangaccio, "Digital wavefront measuring interferometer for testing optical surfaces and lenses," Appl. Opt. **13,** 2693–2703 (1974).
9. J. Li, X.-J. Su, and L.-R. Guo, "Improved Fourier transform profilometry for the automatic measurement of three-dimensional object shapes," Opt. Eng. **29,** 1439–1444 (1990).
10. K. Creath, "Phase-measurement techniques," in *Progress in Optics,* E. Wolf, ed. (North-Holland, Amsterdam, 1988), Vol. XXVI, pp. 349–393.
11. K. Leonhardt, "Topometrie rauher technischer Oberflaechen durch Streifenprojektion in mikroskopischen Strahlengaengen," presented at *Jahrestagung der Deutsche Gesellscahft für augewandte Optik,* Oldenburg, Germany, 21–25 May 1991; T. Ittner, "Strukturierte Beleuchtung für 3-D Topographien im Mikroskop," Ph.D. dissertation (Institut fuer Technische Optik, Universitaet Stuttgart, Stuttgart, Germany, 1989).
12. A. Papoulis, *Probability, Random Variables, and Stochastic Processes* (McGraw-Hill, New York, 1965).